Tomographic mammography using a limited number of low-dose cone-beam projection images

Tao Wu, Alexander Stewart, Martin Stanton, Thomas McCauley, and Walter Phillips[a)]
Rosenstiel Basic Sciences Research Center, Brandeis University, Waltham, Massachusetts 02454

Daniel B. Kopans and Richard H. Moore
Massachusetts General Hospital, Boston, Massachusetts 02114

Jeffrey W. Eberhard and Beale Opsahl-Ong
General Electric Global Research, Niskayuna, New York 12309

Loren Niklason
3301 Carriage Trail, Hillsborough, North Carolina 27278

Mark B. Williams
University of Virginia, Charlottesville, Virginia 22908

(Received 16 April 2002; accepted for publication 16 December 2002; published 6 February 2003)

A method is described for using a limited number (typically 10–50) of low-dose radiographs to reconstruct the three-dimensional (3D) distribution of x-ray attenuation in the breast. The method uses x-ray cone-beam imaging, an electronic digital detector, and constrained nonlinear iterative computational techniques. Images are reconstructed with high resolution in two dimensions and lower resolution in the third dimension. The 3D distribution of attenuation that is projected into one image in conventional mammography can be separated into many layers (typically 30–80 1-mm-thick layers, depending on breast thickness), increasing the conspicuity of features that are often obscured by overlapping structure in a single-projection view. Schemes that record breast images at nonuniform angular increments, nonuniform image exposure, and nonuniform detector resolution are investigated in order to reduce the total x-ray exposure necessary to obtain diagnostically useful 3D reconstructions, and to improve the quality of the reconstructed images for a given exposure. The total patient radiation dose can be comparable to that used for a standard two-view mammogram. The method is illustrated with images from mastectomy specimens, a phantom, and human volunteers. The results show how image quality is affected by various data-collection protocols. [DOI: 10.1118/1.1543934]

Key words: digital mammography, computed tomography, low-dose imaging, tomosynthesis, cone-beam

I. INTRODUCTION

Standard mammography techniques, using either screen–film or digital detectors, suffer from the limitation that despite breast compression, three-dimensional (3D) anatomical information is projected into a two-dimensional (2D) image. Image interpretation requires estimating and discounting the overlap of normal tissue structures that can be mistaken for abnormalities. Especially in radiodense breasts, lesions can be obscured by normal breast tissue. Digital x-ray detectors present the possibility of acquiring multiple low-dose images taken from differing angles to enhance the visibility of features within the breast. The number of 2D cone-beam images required to calculate a 3D reconstruction with isotropic resolution is $N_{\text{complete}}=\pi D/r$, where D is the object diameter and r is the resolution.[1] For example, a 10-cm-diam breast at 0.2 mm resolution (5 lp/mm) would require >1000 images. Such a large number of projections is impractical, not only because of excessive acquisition time, but also because the exposure per projection required for adequate signal-to-noise ratio (SNR) would result in an unacceptably high radiation dose. However, if lower resolution is acceptable in one dimension, the number of images and the dose required to produce diagnostically useful reconstructed images can be dramatically reduced, with a corresponding decrease in the image collection time, and without unacceptable reduction in SNR. We present two general approaches to accomplishing this: (a) recording the projection images at large and/or nonuniform angular increments, and (b) using varying detector resolution (effective pixel size). These two approaches may also be used in combination. The methods reported here are appropriate for applications in which the number of projections is limited by constraints of access or the need to limit the total dose and/or exposure time, and in which anisotropic 3D information is useful. We have developed the method in the context of mammography, but the approach should also be applicable to other x-ray imaging tasks.

Our objective is to record a limited number ($N<N_{\text{complete}}$) of low-dose x-ray projection such that the total radiation dose to the patient is comparable to that used for the two projection views of a conventional mammogram. From these images, a 3D x-ray attenuation distribution is computed in which the high resolution of a standard projec-

tion mammogram is retained in the two dimensions lying in the plane of the compression paddle (defined here as the XY plane), while lower resolution is obtained in the third dimension (defined here as Z). This reconstructed volume can then be decomposed into a set of slices that are less subject to obscuring by tissue structures above and below the slice than a standard mammogram.

As discussed in the following, practical implementation of the method requires: (1) a detector with fast image readout, large area, high resolution, and high detective quantum efficiency (DQE) at low x-ray flux; (2) a specialized gantry that allows acquisition of sequential images over a range of angles at repetition rates of <1 s; (3) a method for immobilizing the breast; (4) a computer(s) with a GHz processor(s) and Gbyte RAM; and (5) image-reconstruction software routines. We found that routines based on constrained nonlinear algorithms provided more useful reconstructions than computationally simpler methods such as filtered backprojection.[2] The computer requirements reflect the need to use these more computationally intensive iterative methods.

For a practical mammography system, the set of N images should be collected in less than $\sim$10 s in order to avoid image blur from patient motion. The need to keep the total acquisition time short, and the time interval required to transfer each image out of the detector, define the number of projections that can be acquired. Because the dose in each x-ray exposure can be only $\sim 2/N$ of the dose for a single standard mammogram, a detector with low noise (including the noise associated with transferring each image from the sensor to a computer) is necessary in order to keep the readout noise from significantly degrading the image quality. For 100 μm resolution in the XY plane (16 bits/pixel), there are 6 M image pixels (12 Mbytes) per image for a 20 cm$\times$30 cm detector, requiring a readout rate of 12r Mbytes/s, where r is the number of projections/s.

Several investigators have sought to develop methods that reduce the number of images required for 3D mammography. Maidment *et al.* used a feature-based image reconstruction method to allow 3D reconstructions from a limited number of views.[3] This technique is useful for high-contrast features such as microcalcifications, but is not useful for imaging soft tissue. Niklason *et al.* described a method, ''digital tomosynthesis breast imaging,'' that uses a small number (7–12) of images.[4] The detector and breast are stationary, and images are collected over less than 180° (typically $\sim$50°) by moving the x-ray source.[5] The images are electronically shifted and added to reconstruct image slices at different depths within the breast, with a depth resolution on the order of 1–2 mm. This method is equivalent to a backprojection method with a limited number of views. However, backprojection has a limited capability for showing low-contrast features, and requires an angular range of more than 180° for a cone beam geometry. Fourier-based reconstruction methods (e.g., filtered backprojection) enhance the contrast, but generate very significant reconstruction artifacts when used with a limited number of projections over a limited angular range.[5] For our study, the patient and mastectomy projection images were acquired using this acquisition scheme, but reconstructed using maximum-likelihood, iterative 3D reconstruction methods.

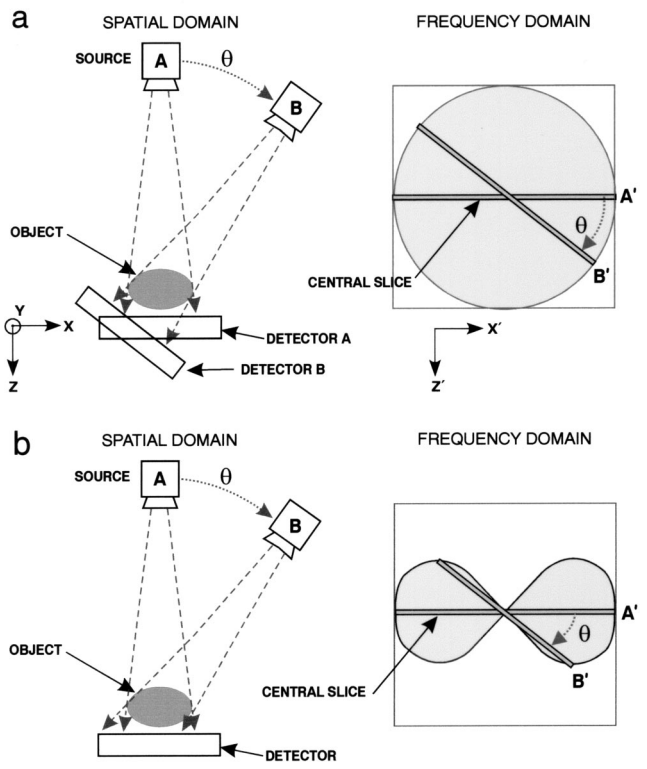

FIG. 1. Schematic drawing of the geometry used for imaging (a) phantoms, and (b) patients and mastectomy samples (tomosynthesis imaging), and the (approximate) relationship of object projections in the spatial domain to central slices in the frequency domain.

II. BACKGROUND

A. Image collection

For the studies described here, digital area x-ray detectors and point x-ray sources were used. According to the central slice theorem,[6] if the distance from the radiation source to the object is infinite, as in the case of parallel beam illumination, the 2D Fourier transform of a single transmission image is equal to a plane through the origin of the 3D Fourier transform of the object. If the distance from the radiation source to the object is not infinite, and the geometry is thus cone beam rather than parallel beam, the above-given description may still serve as a good approximation as long as the cone beam angle and the source rotation angle θ are small ($\lesssim$2°).[7,8] Figure 1 illustrates the relationship between the object projections in the spatial domain recorded by the detector and the central slices in the frequency domain. While Fig. 1 is not strictly valid for larger angles, it does illustrate the information that is collected with the method. Because of the perspective transformation inherent in cone beam imaging, the central slice theorem is not directly applicable to cone beam imaging. The object projection recorded at angular position A corresponds to the central slice A' in the frequency domain, and the object projection recorded at

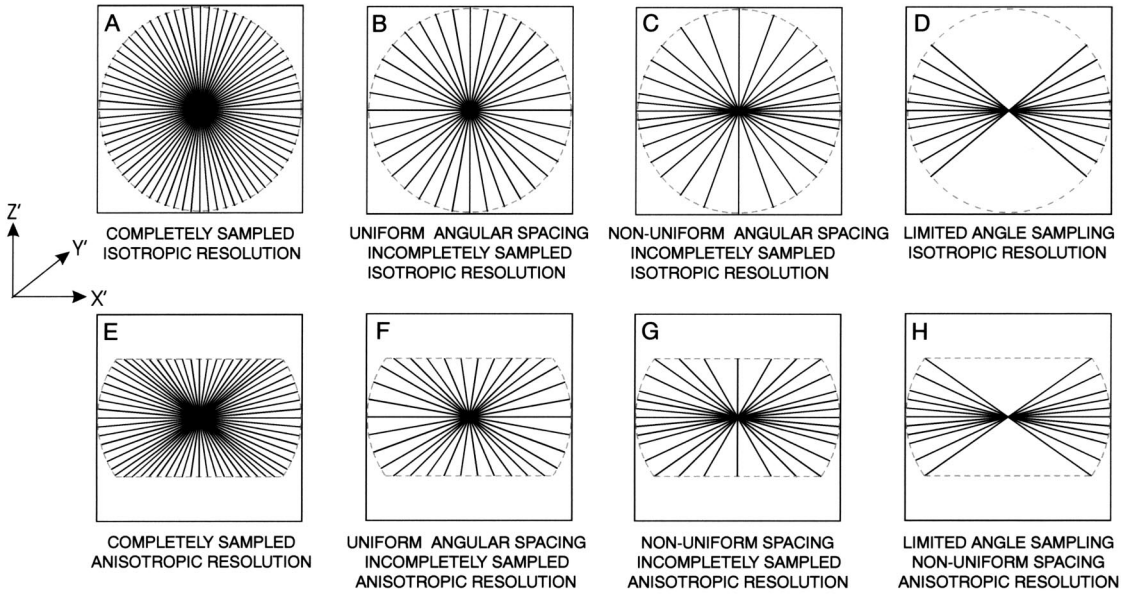

FIG. 2. Representation of *XZ* planes in the frequency domain for (a) completely sampled isotropic resolution; (b) uniform angular spacing, incompletely sampled isotropic resolution; (c) nonuniform angular spacing, incompletely sampled isotropic resolution; (d) limited-angle sampling; (e) completely sampled anisotropic spatial resolution; (f) uniform spacing, incompletely sampled anisotropic spatial resolution; (g) nonuniform spacing, incompletely sampled, anisotropic spatial resolution; and (h) limited-angle, anisotropic spatial resolution.

the angular position B corresponds to the central slice B' in the frequency domain. The high frequency cutoff (i.e., the length of the central slice) is determined by the spatial resolution of the projection data. This is discussed further in Sec. II C.

For the phantom studies described here, the sample was rotated while the detector and x-ray source remained stationary, so that the normal to the detector surface at the center of the detector always intersected the focal spot for all views. This is the acquisition geometry shown in Fig. 1(a). For the specimen and patient studies, the flat panel detector was kept stationary while the tube was moved. This acquisition geometry is shown schematically in Fig. 1(b). Note that, because of the increasing obliquity of the x-ray beam with increasing θ, there is an effective reduction in spatial resolution as θ is increased. This is reflected in the reduced length of the central slice sampled in frequency space. Thus the region of frequency space sampled during the acquisition (the shaded region) is no longer symmetrical, as in Fig. 1(a). Also, the range of imaging angles is limited by the size of the detector and the object-to-detector distance, as indicated in Fig. 1(b). For instance, if an air gap is used with this geometry, the range of angles is reduced. For the specimen and patient studies reported here, the use of an air gap was not investigated. Because the angle between the source and the detector face changes as the detector rotates, the use of a grid is not practical for the geometry in Fig. 1(b).

The disadvantage of taking N low-dose images, each with an exposure of ϵ, as opposed to taking a single image with an exposure of $N\epsilon$, is the increase in total image noise. For a detection system with high noise, such as screen–film (where film granularity noise is significant[9]), relatively high exposures are required to achieve an acceptable SNR in each image, so the aggregate dose becomes high as N becomes large. For a low-noise electronic detector, collecting a large number of images with the same total dose as a single exposure may not significantly degrade the SNR. An example is the low-noise charge coupled device (CCD)-based detector used for the phantom imaging studies. For an exposure of 2000 x-ray photons/pixel we observe a SNR of ~30. For 100 images with the same total dose (20 x-ray photons per pixel per image), the SNR drops only to 25. Thus, using a low noise digital detector, it is possible to collect multiple projections without incurring a large SNR penalty. [The frequency dependent DQE is a more significant measure of detector performance than the SNR. For the CCD-based detector, measurements of the DQE(f) have been made for exposures down to ~900 x-ray photons/pixel through a 3.8 cm acrylic absorber (9 mR entrance exposure),[10] but it is not possible to extrapolate these measurements to very low (~20 x-ray photons/pixel) exposures.] For comparison with images presented in the following, 2000 x-ray photons per pixel in the area under the sample corresponds to an entrance exposure, for the CCD detector, of ~170 mR for the 5-cm-thick phantom, Mo/Mo at 25 kVp, 110 cm source to detector. For the flat panel amorphous silicon detector, 2000 x-ray photons per pixel correspond to an entrance exposure of ~80 mR (14 mrad dose) for a 6 cm breast, Rh/Rh, 30 kVp.

B. Angular sampling of images

The goal of limited, and/or nonuniform angular sampling is to reduce the number of images that must be acquired. Some schemes that could be used to accomplish this are illustrated in Fig. 2. One approach would be to record fewer images of the breast, but at increased angular spacing, such

that the angular range is 360° [illustrated in Fig. 2(b)]. It is plausible that the use of added constraints and iterative methods would allow calculation of a full-resolution 3D reconstruction of the breast with quality equivalent to that derived from Fig. 2(a). A related approach is to image the breast with a nonuniform angular spacing [Fig. 2(c)], or with a limited angular range [Fig. 2(d)]. In the latter two cases, the resultant 3D reconstructions will have anisotropic resolution, with better resolution in the XY plane than in the Z direction. Example images obtained using these approaches are presented in the following.

C. Spatial resolution of images

Variation in the spatial resolution in the projection data from one view to another can be achieved by decreasing the detector resolution as the gantry arm is rotated away from the Z axis. The region of frequency space sampled has the form shown in Fig. 2(e). The example shows projection images obtained with the gantry in the horizontal (XY) plane collected at approximately 1/2 of those obtained with the gantry in the vertical position. Resolution is gradually changed as the gantry is rotated, resulting in the gradually changing cutoff frequency in the resulting central slices [Fig. 2(e)]. If the in-plane resolution (XY) of the projection images with the gantry vertical is 0.1 mm, this corresponds roughly to a reconstructed resolution of ~0.2 mm in the vertical (Z) direction. If instead of the illustrated resolution ratio of 1/2, a ratio of 1/10 were used (with in-plane resolution of 0.1 mm), a 3D map with ~1 mm resolution in the Z direction would be generated. Compared to the example in Fig. 2(a), 1/5 of the dose and approximately 1/2 the number of images would be required, giving a reduction in the imaging time of approximately tenfold. Figures 2(g) and 2(h) illustrate a combined approach where nonuniform angular sampling and nonuniform spatial sampling are both used. Nonuniform spatial sampling is accomplished by binning pixels (summing the signals from an integral number of pixels before signal readout, as described in the following), so for an actual measurement the length of a radial line in Figs. 2(e)–2(h) will depend on the binning factor, and correspond to the Nyquist frequency for the projection data viewed along that particular direction.

D. Exposure per projection and distribution of projections

Uniform angular spacing and equal exposure per image would be optimum if one were attempting to obtain uniform spatial resolution in 3D and the breast were of a symmetrical shape. However, we are not attempting to obtain uniform resolution in 3D, but instead are attempting to limit the radiation dose by using a limited number of views. Because we require high resolution in only two dimensions (X and Y), we need less information about feature detail in the third (Z) dimension. Thus for images made at large angles (large values of θ), the dose per projection (image information content) can be reduced without significantly degrading the quality of the 3D reconstruction. For the same reason, fewer projections need to be made at large angles than at small angles (images close to the XY plane in which high resolution is required). Thus for our purpose it is advantageous to (a) cluster most views near $\theta=0$, and (b) to decrease the exposure for images recorded at large values of θ. This strategy utilizes the total dose more effectively than using a constant dose per image and/or collecting projections at uniform angular increments.

E. Breast geometry

Because we are not relying on only two orthogonal projections to resolve feature overlap, breast compression will not be as critical a factor in our method as it is in standard mammography. It is also clear that with significant breast compression, information content in projections at large angles will be considerably reduced because of the long x-ray path length and consequent high attenuation. We have not done detailed studies of how much breast compression is optimum, but we anticipate that in most cases it will be less than for standard mammography.

F. Reconstruction techniques

Considerable effort has gone into the development of iterative techniques for reconstructions that use a small number of projection images which have low SNRs. Historically, iterative methods have not been used in commercial x-ray tomography systems because they are computationally intensive.[11–13] Iterative methods have found application in nuclear medicine techniques like PET, where the data sets are sparse, the projection matrix size is smaller, angular sampling is less, and there is a large statistical uncertainty because relatively few photons contribute to the projection images compared to transmission CT. Recent improvements in the capacity and speed of computers, coupled with the wider application of image data, have led to iterative techniques becoming popular in image restoration problems.[1,12,14–21] These techniques can be adapted for our problem: low-dose (i.e., low SNR) projection data, and anisotropic angular sampling.

We have used the maximum likelihood expectation maximization (ML-EM) algorithm.[13] This algorithm is not optimal with respect to speed of convergence or computation cost, but it is suited to demonstrating the method and comparing data-collection schemes. Rather than introduce additional complexity to the interpretation of our results, we chose this well-known and well-understood algorithm, and also chose to employ as few additional constraints as possible.

III. METHODS

A. Detectors

Due to practical considerations regarding available equipment, two different acquisition geometries were used for the studies discussed here. They are depicted in Figs. 1(a) and 1(b), respectively. Two types of digital detectors were used in these studies: a CCD-based detector (developed at Brandeis

University, Waltham, MA) for phantom imaging, and the G.E. (GE Medical Systems, Milwaukee, WI) flat-panel CsI amorphous silicon detector for mastectomy specimen and patient imaging. Both detectors have fast readout speeds, low dark current (thermal noise), and low readout noise.

The CCD-based detector has a 10×10 cm area, 1000×1000 0.10 mm pixels (digitized to 16 bits), a Gd_2O_2S:Tb phosphor, a 4.0:1 demagnifying fiber optic taper, 1.5 s readout time, >10 000:1 dynamic range, readout noise of 2 x-ray photons/pixel, and variable spatial resolution (on-chip pixel binning).[22] Binning on the CCD allows the signal in an area of $n\times m$ pixels to be summed prior to readout and then read out as one number. The noise associated with each pixel is composed primarily of two components: read noise (associated with reading out a pixel) and dark noise (thermally induced fluctuations of charge). Because only one read operation is required to read the combined pixels, the readout time is reduced by a factor of $\sim nm$ and the spatial resolution is reduced in both directions. Low dark current (the CCD is cooled to reduce dark current) and short integration times keep the dark noise low relative to the readout noise. Therefore the total noise is dominated by the read noise, and the noise per binned pixel is only slightly greater than the single pixel readout noise. Relative to a detector without binning, the read noise per pixel is lower by $(nm)^{1/2}$.

The GE tomosynthesis prototype mammography detector incorporates a thallium-doped CsI scintillator coupled to an amorphous silicon photodiode array of 1800×2304 detector elements that are 0.10 mm in pitch. The pixel array is read out and digitized to 12 bits in 300 ms by low-noise electronics designed for low-dose imaging. The imager is integrated into a full field digital mammography tomosynthesis prototype system.[23] In this prototype detector, it was not possible to bin pixels before readout.

B. Phantom images

A stereotactic needle-biopsy tissue-equivalent breast phantom (Nuclear Associates, Carle Place, NY, model 18–228) was used to compare data-collection strategies. A 5-cm-thick section of the phantom was sandwiched between two flat carbon fiber/epoxy plates. The section contained low-contrast spherical features 5–8 mm in diameter, and a cluster of higher-contrast features (simulated micro-calcifications) each <1 mm in diameter. Although this phantom has low x-ray contrast targets (except for the simulated calcifications), the images are easy to interpret because there is little overlapping structure and low background structure noise.

The geometry used for imaging the phantom differed somewhat from the geometry used for the patient and mastectomy sample imaging. The source and detector were stationary, and the phantom was rotated. The apparatus consisted of a continuous-output rotating-anode x-ray generator with a 0.2 mm focal spot, Mo/Mo target/filter, computer-controlled x-ray shutter, and computer-controlled rotation stage on which the phantom was mounted 110 cm from the source, with a 20 cm air gap between the phantom and the detector. Both the stage and shutter were controlled by the image collection software, enabling multiple images to be recorded at selected angular increments over a chosen angular range. The stage axis and detector were aligned so that the imaging surface is perpendicular to the line between the center of the imaging surface and the source, and the stage axis is parallel to the imaging surface. We thereby could simulate the cone-beam geometry that would be used for mammography, but had the convenience of rotating the sample rather than the source and detector.

Two series of measurements were carried out in order to show how reconstructions of the simulated microcalcifications differ for three different image-acquisition protocols when the total dose is comparable to that in a standard mammographic study. These two measurement series consisted of a 17-image data set and a 51-image data set. The kVp was held fixed at 25 kV, the milliampere-seconds (mAs) values were ~85 and ~255 mAs, respectively, and the source-to-detector distance was 130 cm. The corresponding entrance exposures were ~330 mR (17-image set) and ~1000 mR (51-image set). To put this in perspective, the single view entrance exposure to a 4.5 cm breast in screen–film mammography using an Mo/Mo target/filter combination and 25 kVp is typically ~800 to 1200 mR. Details of the measurements are given in Table I.

C. Mastectomy images

Two mastectomy samples were imaged with the G.E. flat panel detector and a Rh/Rh target/filter x-ray source, focal spot size 0.3 mm, without a scatter reduction grid (Bucky). The specimens were mounted between a standard compression paddle and the breast support surface, 2 cm above the detector imaging surface in the horizontal plane. The specimen and detector (source-detector distance=66 cm) were stationary and the source was rotated. For the first mastectomy sample (Figs. 6 and 7), the imaging protocol used 9 projection images acquired at 5° increments from −20° to 20°, with a total exposure (integrated over the 9 images) of 45 mAs at 25 kVp, corresponding to an entrance exposure of 266 mR. The data-collection scheme corresponds to that shown in Fig. 2(d), except that even though the detector resolution was fixed (at 0.10 mm), because the detector is stationary the effective resolution varies with viewing angle. The result is that the area of frequency space that is sampled has an oblate shape, rather than the circular shape shown in Fig. 2(d). For the second mastectomy sample (Figs. 8 and 9), 11 projection images were acquired at 5° increments from −25° to 25°, using a technique of 140 mAs and 30 kVp, corresponding to a total entrance exposure (integrated over the 11 images) of 1735 mR. A data set was collected for the mastectomy sample with the 7-mm-thick feature-containing wax insert from an ACR phantom (Gammex RMI, Middleton, WI, Model 156) positioned between the detector and the mastectomy sample. Single projection images of the phantom alone, and the phantom plus mastectomy sample, were also made with the same total entrance exposure.

TABLE I. Details of the data-collection protocols used for the images in Fig. 5. Exposures were made using a Mo/Mo target/filter combination, 25 kVp, source-to-phantom entrance surface distance=110 cm.

Method	Angular range From...To	Number of images	Step between images	Image exposure (mAs)	Binning factor	Total entrance exposure (mR)
			17-image data set			
LA	−17°···17°	17	2.1°	5	1	330
WA	−86°···86°	17	10.8°	5	1	330
NWA						
	−86°, 86°	1, 1		3	8	
	−76°, 76°	1, 1		3	8	
	−65°, 65°	1, 1		3	8	
	−54°, 54°	1, 1		3	8	
	−43°, 43°	1, 1		3	4	
	−32°, 32°	1, 1		6	2	
	−22°, 22°	1,1		6	2	
	−11°, 11°	1, 1		12	1	
	0°	1		12	1	340
			51-image data set			
LA	−18°···18°	51	0.7°	5	1	980
WA	−90°···90°	51	3.5°	5	1	980
NWA	−90°···−50°	12	3.5°	3	8	
	−47°···−36°	4	3.5°	3	4	
	−32°···−18°	5	3.5°	6	2	
	−14°···14°	9	3.5°	12	1	
	18°···32°	5	3.5°	6	2	
	36°···47°	4	3.5°	3	4	
	50°···90°	12	3.5°	3	8	1010
			500-image FBP data set			
FBP	−180°···180°	500	0.72°	36	1	7.7×10^4

D. Patient images

More than 250 patients have been imaged under IRB approval following informed consent. The images from the two patients presented here were acquired with the same geometry as that used for the mastectomy samples. For each breast, 11 images were acquired in a total time of 7 s as the source was rotated in 5° increments over a 50° angular range. The exposure times were ~0.1 s and the time to move the source (during which time the image was read out) was 0.6 s. Medio-lateral oblique (MLO) positioning was utilized, with a Rh/Rh target/filter combination, and technique factors of 28 kVp and 10 mAs per exposure for patient 1, and 30 kVp and 13 mAs per exposure for patient 2. The mean glandular dose (integrated over the 11 exposures) was 307 mrad for patient 1 and 382 mrad for patient 2. The mean glandular dose in a conventional mammogram for patient 1, recorded with a Mo/Mo target/filter combination at 25 kVp, was 330 mrad (per exposure).

E. Reconstruction methods

Maximum Likelihood (ML) is a family of iterative reconstruction methods.[11] The objective is the likelihood function L, which is the probability of getting the projections Y obtained in the experiment, given a 3D model of attenuation coefficients u:

$$L = P(Y|u). \tag{1}$$

The solution is the reconstruction model that maximizes the probability of getting the measured projections. Because an analytical solution to ML is usually intractable, iterative algorithms are generally used. If the incident and transmitted x-rays follow Poisson statistics, the likelihood is described by[24,25]

$$L = \prod_i \{P_i(Y_i|u)\} = \prod_i \left\{ \frac{e^{-\bar{Y}_i}\bar{Y}_i^{Y_i}}{Y_i!} \right\}. \tag{2}$$

The likelihood associated with the measurement of each detector pixel is $P_i(Y|u)$, and the multiplication is over all pixels. Y_i is the measured number of x-ray photons in the image at projection pixel i. In our reconstruction problem $\bar{Y}_i$ corresponds to the calculated number of photons based on the attenuation model u,

$$\bar{Y}_i = D_i e^{\langle l,u\rangle_i} \tag{3}$$

is the mean number of photons in the pixel; D_i is the number of incident x-ray photons at projection pixel i before attenuation; $\langle l,u\rangle_i = \Sigma_j l_{ij}u_j$ is the total attenuation along the beam ray to pixel i; and l_{ij} is the intersection length of beam ray i and the model voxel j. $P_i(Y|u)$ describes the Poisson probability of the measured number of x-ray photons Y_i with the mean calculated pixel value $\bar{Y}$. The log likelihood is then[7]

$$\ln L = \sum_i \left(-D_i e^{-\langle l,u\rangle_i} - Y_i \langle l,u\rangle_i + Y_i \ln D_i - \ln(Y_i!) \right). \tag{4}$$

The assumption implicit in this formalism is that the recorded intensity is related to the log of the integral of the attenuation along the path. This assumption is not strictly true because (a) there is scatter and (b) the x-ray beam is not monochromatic. In fact, scatter may account for a significant portion of the recorded signal, particularly in highly attenuating regions. These effects are ignored in the algorithm we use here, and we do not investigate the effect of scatter and beam hardening in this report. There is also an uncertainty introduced in the measured value of Y_i due to the fact that our detectors are integrating detectors, not photon counters, but this uncertainty is small compared to the uncertainty due to photon counting statistics for these measurements. Scatter and beam hardening are the dominate causes of the error in the measurement of transmitted photons.[2]

The transmitted x-rays collected by the detector are ''incomplete information'' about the attenuation coefficient of image voxels along the beam ray. This makes it difficult to solve the ML equations using conventional approaches because these methods, such as the gradient-based method,[26] will lead to a large number of insoluble simultaneous equations. The expectation maximization (EM) algorithm embeds the observed ''incomplete data'' Y into a larger unobserved ''complete data'' space. For a single projection data pixel from the ''incomplete'' (but observed) data space Y, this complete data space consists of the unobservable x-ray counts leaving each voxel along the beam ray from the source to the projection image pixel $\{X_0, X_1, X_2, \ldots, X_{m-1}, X_m | X_m = Y\}$. In this ''complete data'' space it is simpler to find the solution to ML.[11,27] Because the ''complete data'' are not known, the EM algorithm uses their expectation based on the current estimate of the model.

There are two steps at each iteration of the EM algorithm: an expectation step (E-step) and a maximization step (M-step). In the E-step, the ''complete data'' are estimated by calculating their expectation, given the ''incomplete data'' Y and the current model $u^{(n)}$. In the M-step, the log-likelihood function of the ''complete data'' is maximized, assuming the estimated ''complete data'' from the E-step are correct. The log-likelihood function based on expectation of ''complete data'' is represented by the function $Q(u|u^{(n)})$,

E-step: compute $Q(u|u^{(n)})$ using Y and $u^{(n)}$.

M-step: find $u^{(n+1)} = \text{argmax}\{Q(u|u^{(n)})\}$.

Iterative execution of these steps leads to the model u that maximizes the likelihood function of the measured ''incomplete data.'' In effect, the EM algorithm reduces the complexity of solving the log-likelihood function by replacing it with $Q(u|u^{(n)})$. The ML method asks for the model that would give the observed data with the highest probability. This is hard to evaluate directly without testing all possible models. The EM approach asks for the maximization of the function Q given a current model. This takes the current model and improves it incrementally in the maximum likelihood direction. In order for the iteration not to converge to a local optimum, the reconstruction problem has to be ''convex,'' that is, there are no models that cannot be incrementally improved (no local maxima). In this case the iteration process will always approach an ''answer.'' (Shepp and Vardi[28] showed the ML reconstruction problem to be ''convex'' in the case of emission tomography, Lange and coworkers showed the transmission tomography case to be ''convex,''[11,13] although constraints could affect this conclusion). We do not iterate to convergence, so the ML model itself is not reached. The path which the algorithm takes is therefore important, as is number of iterations before stopping the algorithm.

Additional information can be used to constrain the solution and produce a more meaningful reconstruction. To apply constraints, a term is added to the objective function:

$$P(u) = \log L(u) + \lambda V(u), \tag{5}$$

where $P(u)$ is the new objective function, $V(u)$ is the constraint function, and λ regulates the strength of the constraint. The solution maximizes the objective function $P(u)$. We use two constraints, non-negativity and a maximum attenuation coefficient ($0 \leqslant u \leqslant 1\ \text{cm}^{-1}$). Other constraints typically affect the appearance of the reconstruction. For example, a constraint on the pixel-to-pixel fluctuation in the reconstruction can reduce noise, but will also reduce spatial resolution.

In our implementation of the ML-EM reconstruction technique of Lange and Fessler,[13] the attenuation coefficients in the model were updated with the following:

$$u_j^{(n+1)} = u_j^{(n)} + \Delta u_j^{(n)}, \tag{6}$$

$$\Delta u_j^{(n)} = \frac{u_j^{(n)} \Sigma_i l_{ij} (D_i e^{-\langle l,u^{(n)}\rangle_i} - Y_i)}{\Sigma_i (l_{ij} \langle l,u^{(n)}\rangle_i D_i e^{-\langle l,u^{(n)}\rangle_i})}. \tag{7}$$

The numerator of the voxel update Δu_i is proportional to the attenuation in the voxel, thus the update is multiplicative. (A zero in a voxel will never change, and should be avoided when initializing the model.) The summed expression in the numerator represents the backprojection of the difference between the expected intensity ($D_i e^{-\langle l,u\rangle_i}$) and the observed intensity Y_i, in the projection images. This ''error term'' is backprojected into the voxel by multiplying by l_{ij} (the intersection of each projection ray with the voxel being updated). This error is weighted by the factor in the denominator, which provides the minimum expected error under the assumption of Poisson noise in the observed projections. We did not find it necessary to go beyond the classic implementation of Lange and Fessler,[13] despite there being significant deviations from the assumptions under which they derived the algorithm.

The contribution to the voxel update from each projection is proportional to the number of incident x-ray photons D_i. In imaging the phantom, the number of incident x-ray photons varied with angle. At each angle, the bare-beam inten-

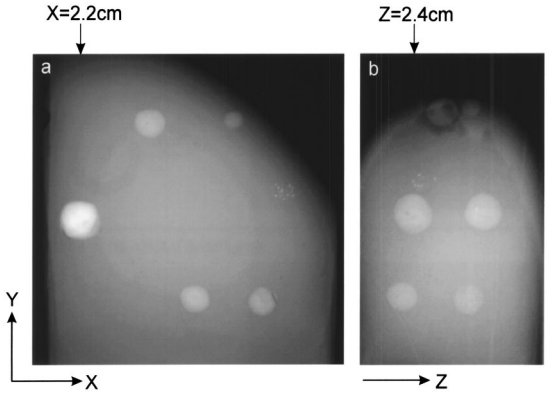

FIG. 3. Two orthogonal projection views of the phantom made at 25 keV, Mo/Mo, 110 cm source-to-phantom, 130 cm source-to-detector, 400 mAs (equivalent to 100 mAs at 65 cm source-to-detector). One of the simulated masses is obscured by another in the *XY* view. The arrows indicate the location of the layers shown in Fig. 4.

sity was measured in an area outside of the object shadow, and used as D_i at this angle in Eq. (7).

IV. RESULTS

A. Phantom images

A phantom designed for teaching stereotactic needle biopsy is used to illustrate methods for collecting multiple-image data. Two orthogonal projection views of the phantom are shown in Fig. 3. The simulated microcalcifications are visible at the right center of Fig. 3(a).

The schemes presented in Fig. 4 illustrate alternative image-collection strategies. The two right columns of Fig. 4 show 2-mm-thick slices in two orthogonal directions from ML-EM 3D reconstructions based on 3 different data-collection protocols (rows 1–3), and the same layers calculated from a FBP reconstruction from 500 equally spaced, equal-exposure images made over 360° (row 4). The 500-image set is included in order to generate ''truth'' images for comparison with the lower-dose images. The drawing in the left-hand column represents the source and detector positions and the relative entrance exposure per projection (for the actual measurements the sample was rotated).

The area of the *XY* plane shown in Fig. 4 contains one simulated mass sphere and simulated microcalcifications. [The edge of a second sphere is just visible in this plane, Fig. 4(d)]. The orthogonal *YZ* plane contains two spheres that overlap one another in the *XY* plane. Comparison of the four *XY* and *ZY* images illustrates some of the tradeoffs associated with the each protocol. The limited-angle reconstruction results in good image quality in the *XY* plane, but poor resolution in the *YZ* plane. The uniform wide-angle sampling results in improved resolution in the *YZ* plane, but close inspection shows that image quality in the *XY* plane is somewhat degraded, as judged by the loss of detail in the calcifications and the increase in noise. The uniform wide angle sampling protocol provides the best *Z* resolution because more views are obtained where the angle between the plane of the detector surface and the *YZ* plane is small. The nonuniform, wide-angle sampling is a compromise that yields moderate resolution in the *YZ* plane while maintaining good image quality in the *XY* plane. All of these sampling protocols result in the ability to visualize the location of features in 3D.

Figure 5 shows reconstructed 1-mm-thick layers in the *XY* plane at 3 *Z*-axis levels for the area around the simulated microcalcifications. Here *Z* resolution is most easily visualized by looking at the structure artifacts evident in the $Z=13$ mm layers, where there are in fact no simulated microcalcifications in the phantom. Judging from Fig. 5, limited angle sampling (LA) results in good resolution of detail in the plane, but poor resolution in *Z*. Uniform wide angle sampling (WA) results in reduction in the in-plane (*XY*) resolution, and good resolution in *Z*. Nonuniform wide angle sampling (NWA) with nonuniform exposures and binning results in resolution in the *XY* plane that appears nearly as good as that for limited angle sampling, and in relatively good resolution in *Z*. For the lower dose series, these differences are more pronounced.

B. Mastectomy images

Images of a mastectomy specimen are show in Fig. 6. The figure demonstrates one way in which a low-dose 3D data set can be processed to increase the conspicuity of microcalcifications over that provided by a single transmission mammogram. Figure 6(a) shows the low-dose transmission image recorded at 0°. From the 3D attenuation distribution reconstructed from the 9 images in the data set, the maximum intensity projection (MIP) at 0° and the mean intensity projection at 0° were calculated at every pixel position. The difference between the two images (MIP minus mean intensity projection) is shown in Fig. 6(b).

Three 2-mm-thick slices in a 4×4 cm area of the reconstruction are shown in Fig. 7. Eight iterations were used. One hundred 0.4-mm-thick slices parallel to the *XY* plane were calculated in the reconstruction; these were subsequently binned in groups of 5 to give twenty 2-mm-thick slices. The effective pixel size in the image plane is 0.10 mm. Features are clearly separated into different vertical layers with a depth resolution of 2 mm. The calcifications due to high-grade ductal carcinoma *in situ* delineate a segment of the ductal network of the breast. Some of the microcalcifications observed in the $Z=28$ mm layer appear to be localized within the layer and are not visible in the adjacent $Z=30$ mm layer, while others are either spatially extended or located near the boundary between layers. At the $Z=36$ mm layer, no microcalcifications are apparent.

The results of the phantom plus mastectomy imaging experiment shown in Fig. 8 demonstrate how the method can remove overlapping structure to reveal features in a layer. In the 0° projection image [Fig. 8(b)], features in the phantom are difficult to visualize due to structure in the mastectomy sample. Only the highest-contrast cluster is obvious. In the reconstructed phantom layer [Fig. 8(c)], the structure noise of the mastectomy sample is removed and many of the phantom features can be seen, although reconstruction artifacts

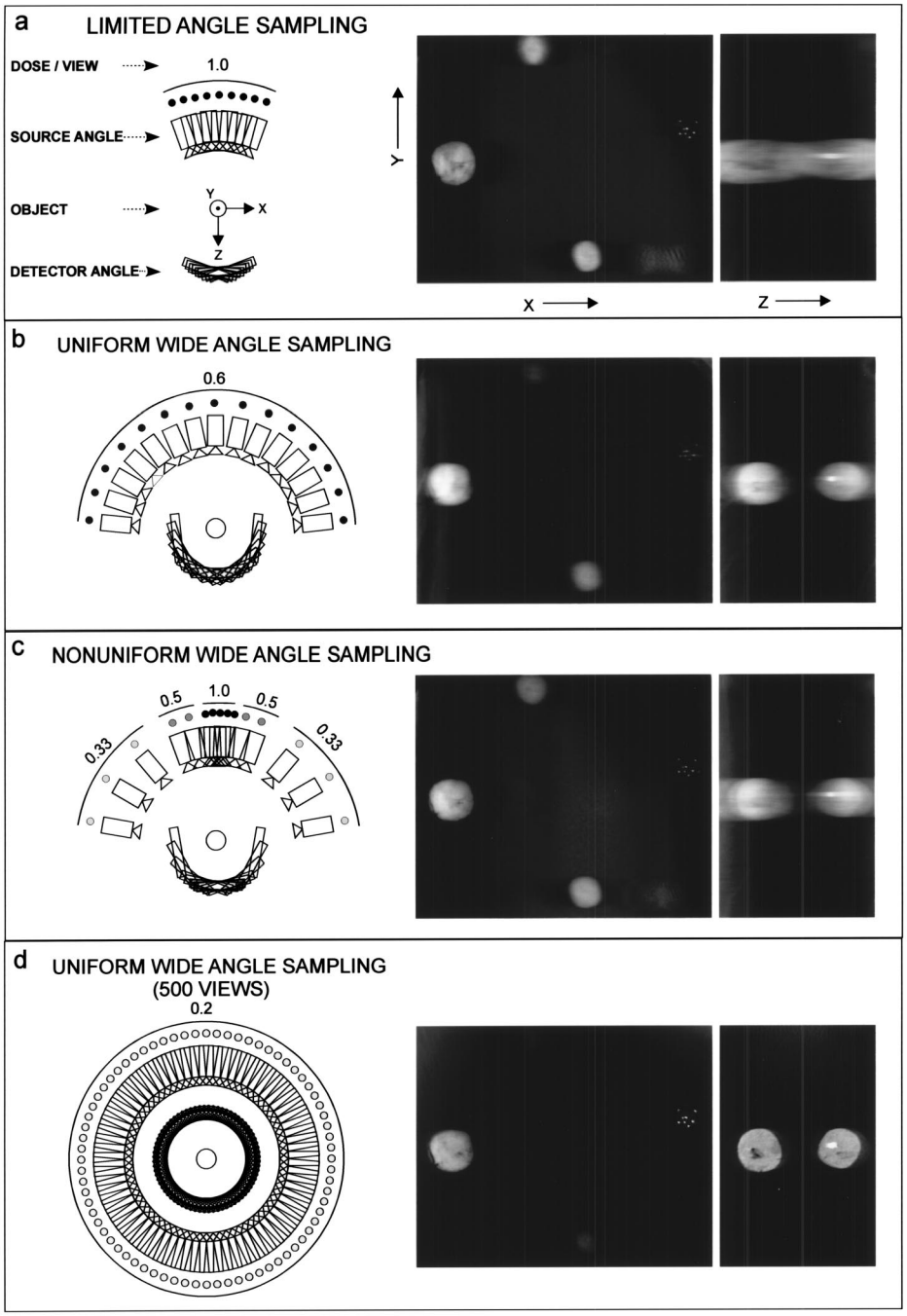

FIG. 4. Image acquisition protocols for 3D imaging of the phantom; (a) limited angle sampling; (b) uniform wide angle sampling; (c) nonuniform wide angle sampling; (d) 500-image uniform sampling over 360°. For (a), (b), and (c), images were collected at the angles and relative entrance exposures indicated in the drawings in the leftmost column; the total entrance exposure in each of the 3 data sets was to 1800 mAs at 25 keV, Mo/Mo, 110 cm source-to-phantom distance, corresponding to a total entrance exposure of 6.9 R. In (a) 9 images 5.4° apart were used (corresponding to the geometry used for the mastectomy images); in (b) 15 images 12.6° apart were used; in (c) 15 images at different angles, exposures and binning factors were used; in (d) 500 images were used resulting in a total entrance exposure of 77 R. In the coordinate system shown, the *Y* axis is vertical and the detector imaging plane is normal to the *Z* axis at 0°. Two orthogonal 2-mm-thick layers through the reconstructions are shown for each sampling protocol. The layers are located at the *X* and *Z* depth positions indicated by the arrows in Fig. 3. The brightness and contrast of the images displayed have been manipulated in order to show details in this inherently low-contrast phantom.

from features in the mastectomy sample still obscure low-contrast features in the phantom.

For the reconstructed layer, the contrast, the variance in the background (σ^2), and the differential signal-to-noise ratio (SNR), were measured as a function of the number of iterations. The contrast $C=(N_{\text{feature}}-N_{\text{background}})/N_{\text{background}}$, where N is the average attenuation value. For the calcifications, the maximum pixel value in each feature was used to calculate N_{feature}. The maximum pixel value was used, even though noise is introduced by selecting only one pixel value, because the calcifications are small (in the reconstructed image a calcification consists of ~10 voxels and has an irregular shape), so the values of pixels adjacent to the central pixel were generally considerably lower. The relative variance of the background [Fig. 9(a)] was evaluated for a 100×100 pixel area of the image slice of the phantom [wax insert, Fig. 8(c)] in which we assume the attenuation is uniform. The average SNR for the 3 sets of simulated calcifications and for the largest simulated mass visible in the phantom [Fig. 8(a)] were calculated by evaluating $\text{SNR}=(N_{\text{feature}}-N_{\text{background}})/\sigma$. As shown in Fig. 9(b), for a small number of iterations, the contrast of a relatively large, low-density feature (mass) increases faster than the contrast of a smaller, high-density feature (calcification). For the mass, the SNR

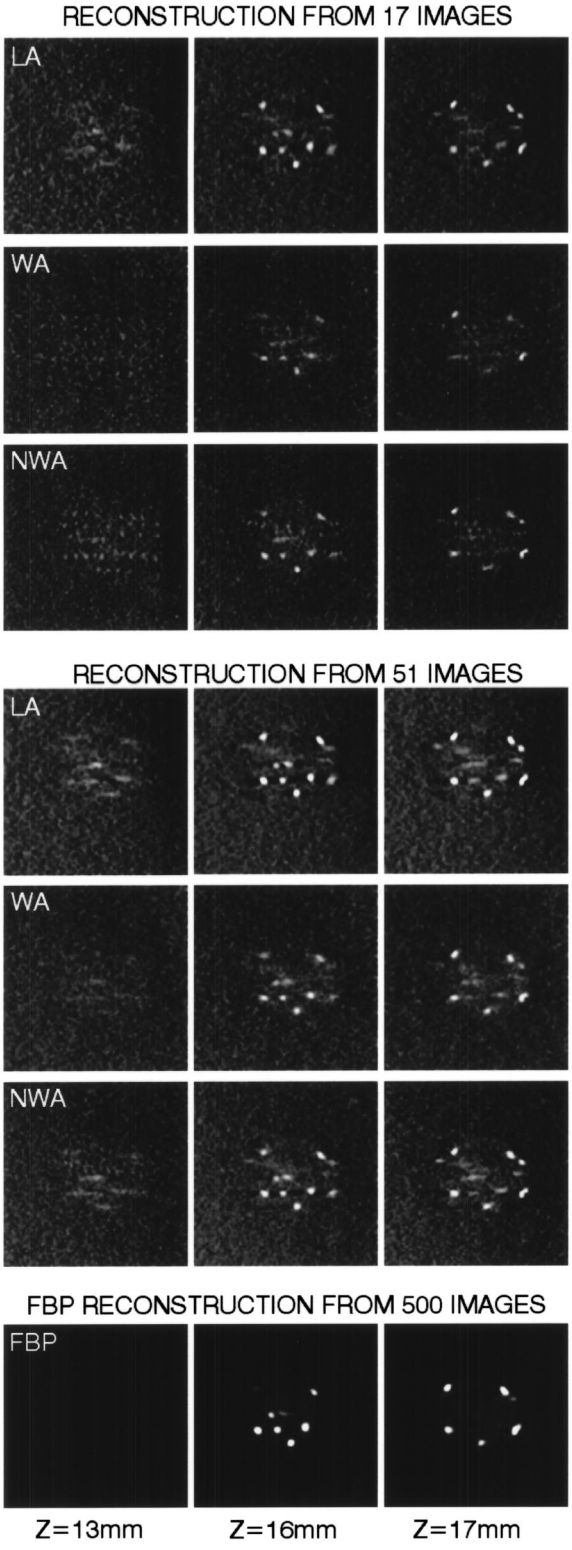

FIG. 5. Simulated microcalcifications in 1-mm-thick density layers reconstructed from phantom images collected with the sampling schemes detailed in Table I: limited-angle sampling (LA); wide-angle sampling (WA); nonuniform wide-angle sampling (NWA); and filtered backprojection (FBP). Layers at 13, 16, and 17 mm from the phantom surface are shown for each of the sampling schemes. Each data set in the first series of image layers consisted of 17 exposures with a total entrance exposure (sum of 17 radiographs) of ~330 mR. In the second series of images, there are 51 exposures with a total entrance exposure of ~980 mR.

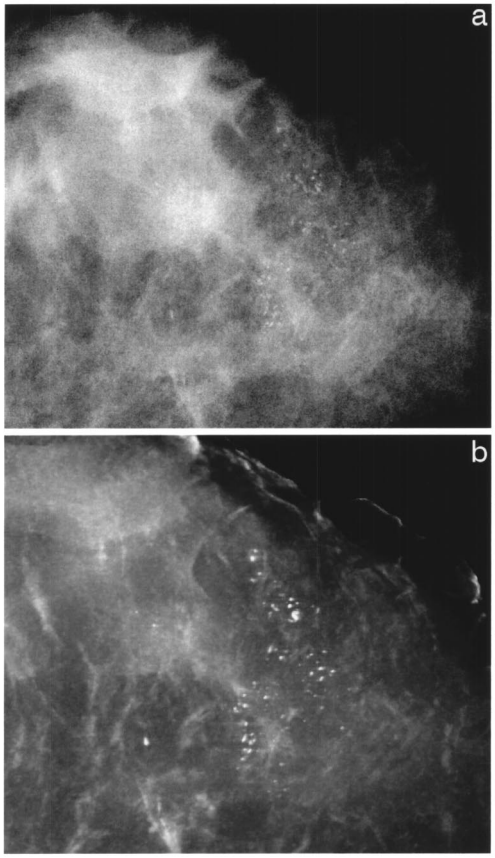

FIG. 6. (a) Low-dose projection image recorded at 0° from a 10×14×4 cm mastectomy specimen. (b) Difference between the 0° maximum intensity projection and the 0° mean intensity projection images derived from the reconstruction. The relative brightness and contrast have been adjusted to enhance features of interest.

[Fig. 9(c)] does not increase after 3 iterations because high-frequency noise present in the data is overfit by the algorithm. With further iterations, the magnitude of the amplified noise increases faster than the improvement in feature contrast and the SNR decreases. The amplification of noise is a characteristic of nonregularized algorithms such as the ML-EM algorithm. We chose the ML-EM algorithm for this study because it is well-known and well-understood; in clinical use some form of regularization could be used to suppress noise.[13,29,30] The results correspond to our qualitative assessment that the conspicuity of most features in the reconstructed layers of mammograms is optimized by 8–10 iterations. Although the contrast and SNR are measured numbers, the curves in Fig. 9 are smooth because they are given by a deterministic calculation, and therefore do not reflect the error in the reconstructed image due artifacts caused by out-of-plane structures. Since the phantom is uniform, the error in the reconstruction is reflected by the increase in the background variance. Figure 9 is presented to demonstrate the convergence behavior of the algorithm for small and large features; a different phantom and sample would give different values for contrast and SNR, but the general features of the curves would be repeated.

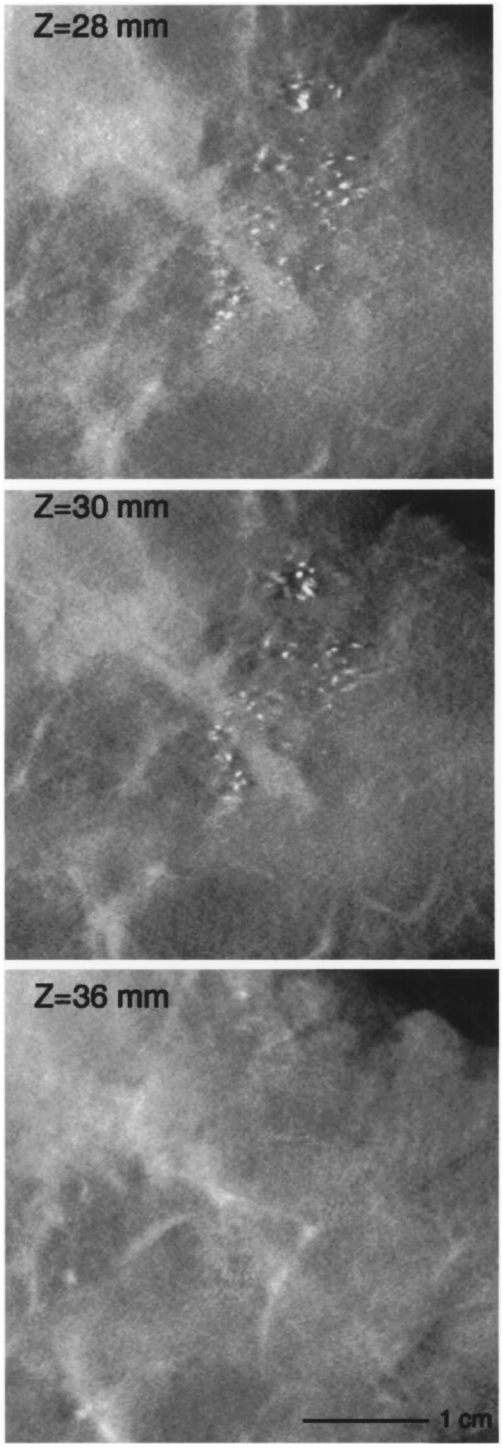

FIG. 7. Reconstructed density layers of a 4×4 cm area of the 4-cm-thick mastectomy specimen shown in Fig. 6, using the same 9-image data set. Layers 2 mm thick at 28, 30, and 36 mm levels in *Z* are shown.

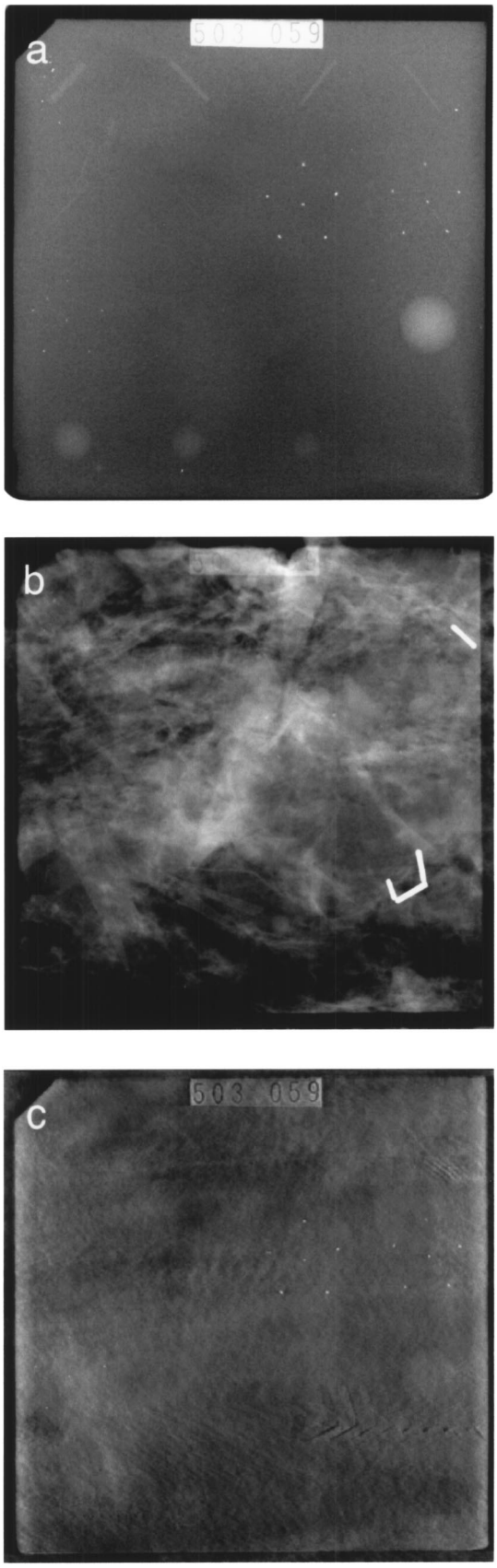

FIG. 8. (a) Projection image of the wax insert from an ACR breast phantom. (b) Projection image of the wax insert positioned under a 5.5-cm-thick mastectomy sample; (c) 2-mm-thick density layer reconstructed from the 11-image data set of the phantom/mastectomy sample.

C. Patient images

The patient whose images are shown in Fig. 10 was found to have a nonpalpable 10 mm invasive ductal cancer with associated *in situ* tumor. Blood vessels are visible near the breast surface in layer (a). A tumor that has intraductal as well as invasive ductal cancer elements is just out of the

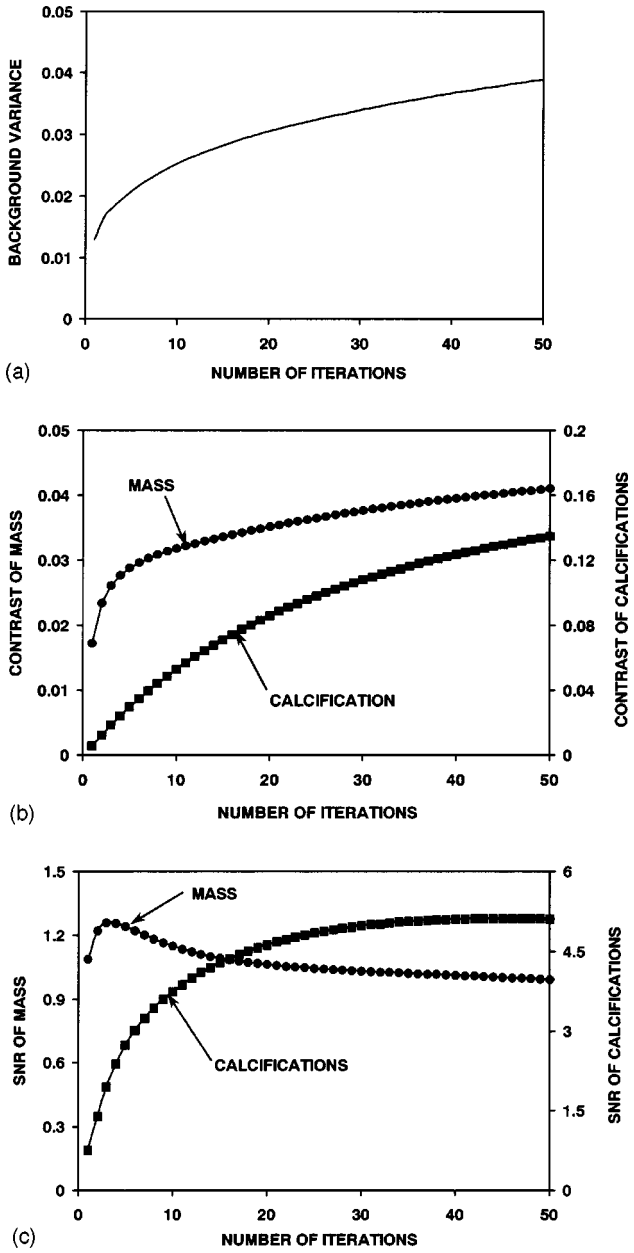

FIG. 9. (a) Variance in the background. (b) Contrast and (c) SNR of the large mass and simulated calcifications in the reconstructed layer shown in Fig. 8(c). In (a), artifacts caused by features in the mastectomy sample contribute to the background variance. The standard deviation in the average background intensity is <3% at 10 iterations and <4% at 50 iterations.

plane of layer (b). The invasive tumor mass (arrow) with associated calcifications in the *in situ* portion is clearly seen in layer (c), as is a benign, intramammary lymph node in the upper portion of the image. The cancer is difficult to see in the conventional screening mammogram [film/screen technique, Fig. 10(d)], and was found primarily because the calcifications associated with it drew the attention of the radiologist.

Figure 11 shows 5-mm-thick MLO reconstructed layers at two levels separated by 14 mm in each breast of patient 2. Images L(a) and R(a) show areas of architectural distortion in the plane of sections from previous breast biopsies. Features that are clearly visible at level (a) are not present at level (b), demonstrating the separation into layers that enhances the conspicuity of features. In Fig. 11 R(a), the higher voxel value at the periphery of the lesion in the same plane indicates a fatty central region. This suggests that the lesion is not malignant, since a malignant lesion would have a more dense central region. Preliminary analysis also suggests that the conspicuity of the calcifications is markedly increased.

In some of the reconstructed images, artifacts caused by high-contrast features arise because of the limited number of projections used for reconstruction. Metal clips produce the artifacts shown in the upper-right and lower-right of Fig. 8(c); calcifications produce the artifacts shown at the center left of image Fig. 11 L(b); and uncorrected bad pixels produce the 6 dark dots on the top right of images Fig. 11 L(a) and L(b). These artifacts can be recognized because they are discrete, repetitive ghost features aligned along the x-ray trajectory and they converge to a true high contrast feature in one image plane.

V. DISCUSSION

The straightforward technique of processing the 3D attenuation information at each voxel illustrated in Fig. 6 provides diagnostically useful information that cannot be extracted from two standard (MLO, CC) mammography images. The reconstructed density layers from a mastectomy specimen and two patients (Figs. 7, 8, 10, and 11) demonstrate that 3D reconstructions from a limited number of low-dose x-ray images are useful for detecting features in three dimensions, and thus can resolve ambiguities which may arise from the overlap of structures in standard two-view projection mammography.

For the patient studies, the 11 exposures were equally spaced over 50°. The finite size of the detector and use of full breast compression limited the angular range. Data-collection schemes that allow both the detector and source to rotate, similar to those we have presented for imaging the phantom, may lead to improvement of the technique for screening and diagnostic mammography. These schemes would use a specialized gantry and incorporate wider-angle sampling and nonuniform entrance exposure, nonuniform angular spacing, and possibly variable-resolution imaging (binning).

Only that volume of the breast that is illuminated from all angles can be reconstructed. Although we have not yet experimented with large angle (greater than 25°) views in a clinical context, we anticipate few if any problems associated with obstruction of structures near the chest wall. Patients will likely be positioned as in a standard cranio-caudal view, so even at large viewing angle their arms and shoulders would not be in the x-ray beam. A thin barrier between the patient's abdomen and the detector would assure that detector motion would not result in patient motion. Introduction of the thin barrier would result in the loss of a small amount of imaged tissue near the chest wall. Depending on the relative position of the patient and the detector, the nonimaging

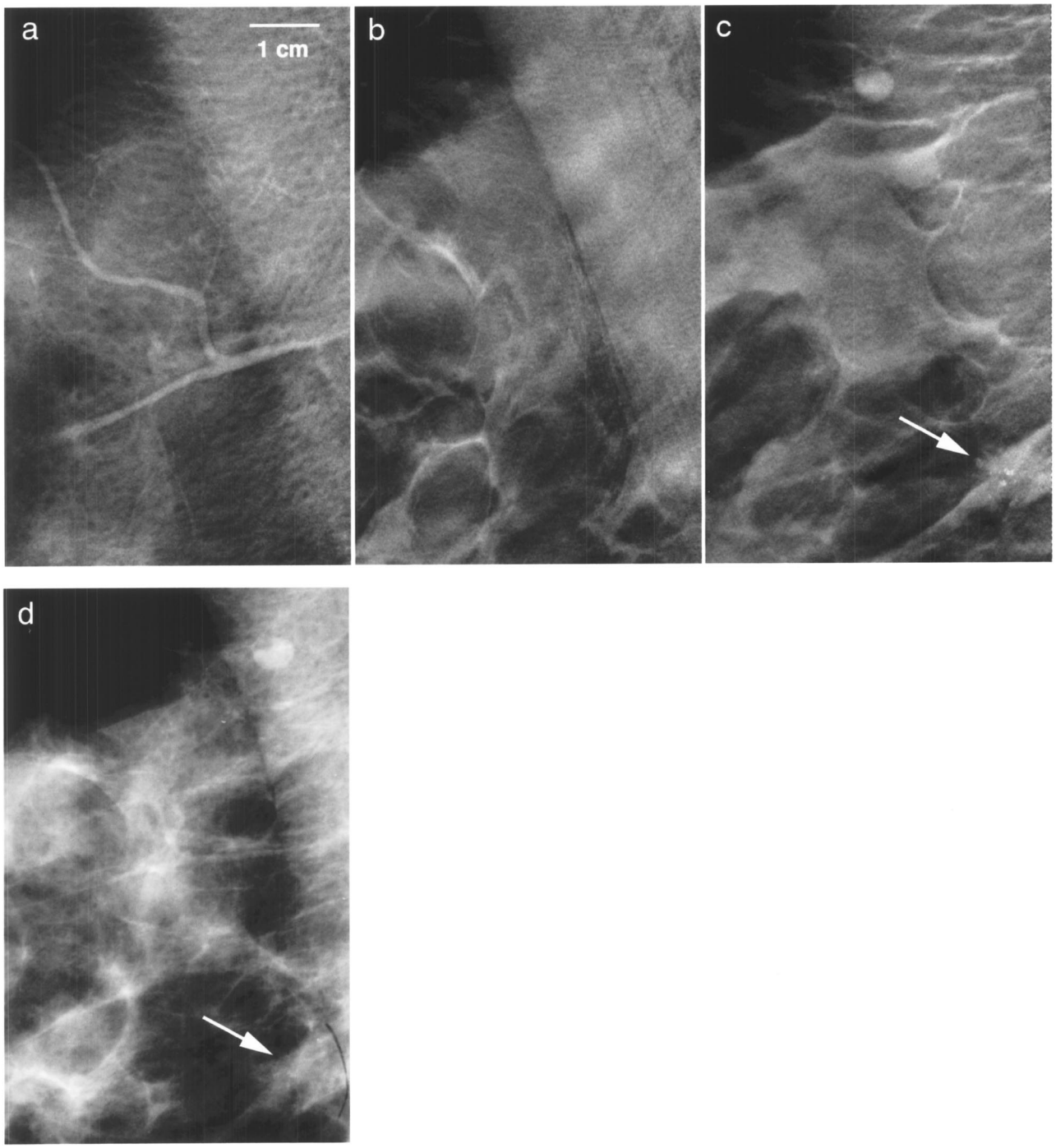

FIG. 10. (a), (b), and (c): Reconstructed layers of density at 3 levels obtained from mediolateral oblique projection images from a volunteer (patient 1). Each reconstructed layer is 2 mm thick. The layers are at: (a) 2 mm, (b) 22 mm, and (c) 32 mm from the breast surface (compression paddle), and the compressed breast thickness was 5 cm. A corresponding area from the digitized screening mammogram of the same patient, recorded with film/screen, Mo/Mo, 25 kV, 330 mrad mean glandular dose, is shown in (d).

frame of the detector could also obscure the image near the chest wall.

We have not endeavored to determine the minimum number of views required to provide sufficient Z resolution. Many factors would be involved in making that determination, including the dose limit, the angular range over which projections are acquired, the amount of compression, the x-ray energy, characteristics of the detector, and the reconstruction algorithm.

Since high-frequency noise in the data is amplified by each iteration of the reconstruction algorithm, fewer iterations may be optimum for the detection of low contrast objects such as small masses. However, the conspicuity of a low-contrast feature will in part depend on the detection of the feature's edges, and this will involve higher-frequency information. Curves such as those in Fig. 9 cannot by them-

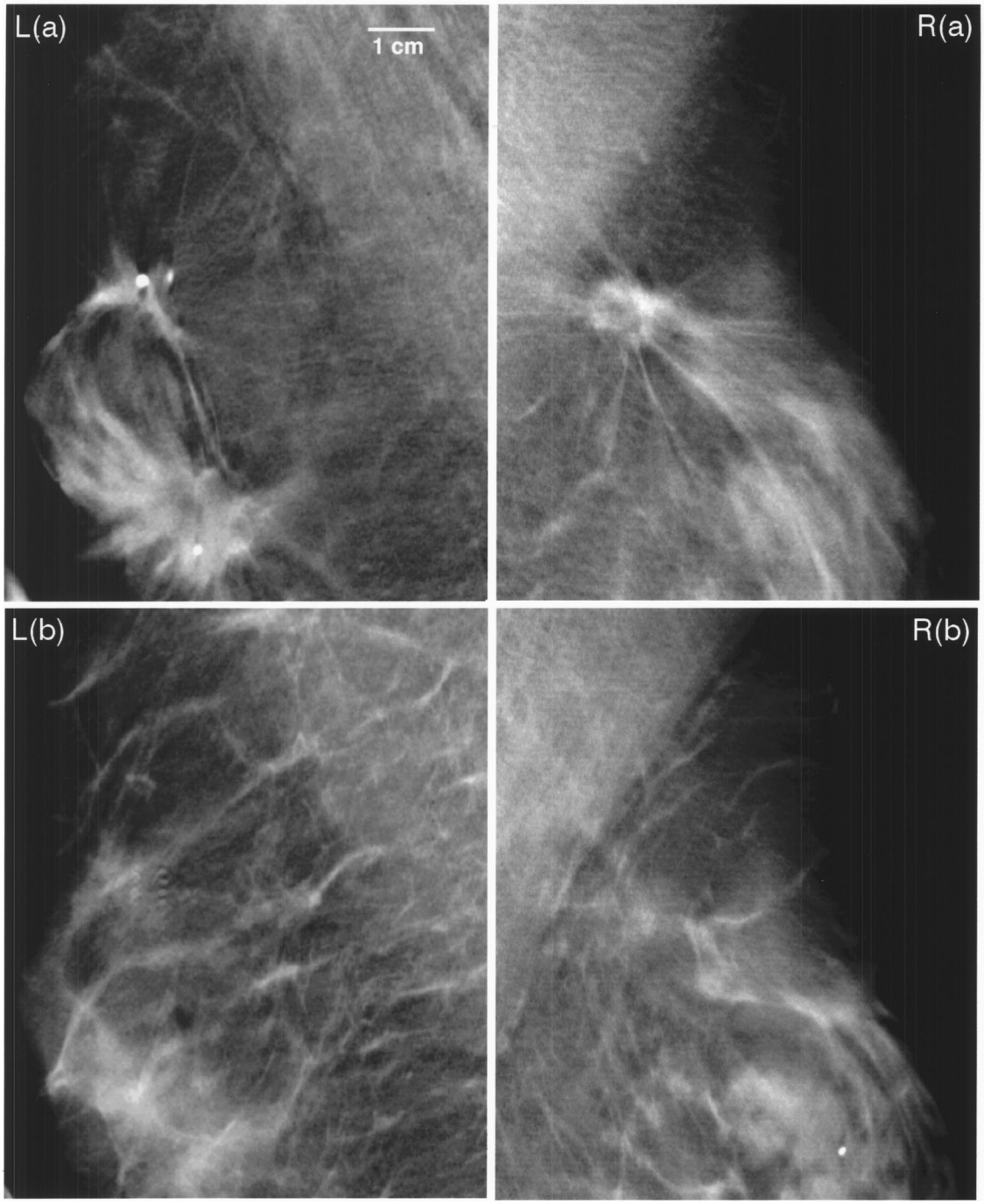

FIG. 11. Images of 5-mm-thick layers from reconstructions of the left (L) and right (R) breasts of a volunteer (patient 2). The compressed breast thickness was 6 cm. The layers are at levels: L(a) 28 mm; L(b) 42 mm; R(a), 16 mm; R(b), 30 mm from the breast surface (compression paddle). Figures L(b) and R(b) are layers away from the sections containing the scars.

selves answer the question of what is the optimum number of iterations. Our experience with ~250 patient cases (500 images of left or right breasts) using a nonregularized (ML-EM) algorithm has been that most features are visible after 2 or 3 iterations; details such as tumor edges are conspicuous after 2 or 3 more iterations. Radiologists have found that 8–10 iterations generally give reconstructed images with sufficient feature contrast and detail, and that increasing the number of iterations much beyond 10 does not improve image quality. The optimum number would be best determined by a controlled multi-reader study.

For the patient imaging studies, there was no air gap between the detector and the breast. An air gap could be used to reduce scatter if the detector is rotated with the source. Wu has shown in simulated mammography experiments that increasing the scatter-to-primary ratio by a factor of 2 decreased the signal-to-noise in the reconstruction by roughly a factor of 2.[2] Although we have not done it here, scatter mod-

eling can be included in the computation of the forward projection data.[31–33] Despite the considerable contribution of scatter to the projection images, we found that we could successfully apply the ML-EM algorithm.

When collecting images for 3D reconstruction, some form of breast stabilization is essential to keep the breast stationary. However, if images are to be recorded over a wide range of angles, full compression may not be required or even optimal. X-ray attenuation through the long axis of a fully compressed breast is too high to allow low-dose wide-angle imaging (unless the x-ray energy is significantly higher than that used for conventional mammography). Although we have not studied the correlation between the amount of compression, the range of imaging angles, and the quality of the reconstructed images, we anticipate that at least in some cases, reduced compression will be practical. Even with reduced or minimal compression, resulting in a less flattened breast shape, nonuniform angular sampling and/or varying detector resolution may still be advantageous, because we are looking for high resolution in the *XY* plane and lower resolution in *Z*. Reduced compression would reduce patient discomfort, and might encourage more women to be screened routinely for breast cancer.

The x-ray energies used for conventional mammography (Mo or Rh targets operated at 25–35 kVp) are optimized for a configuration where the compressed breast is viewed at normal incidence and images are recorded with a screen/film-based system. Since we are using a digital detector and the images are processed rather than viewed directly, we are more concerned with the information content of our images than with the appearance and contrast. We have modeled the information content (SNR) as a function of energy at constant dose. Using the exponential relation between x-ray absorption and photon counts [Eq. (3)] and the Poisson statistics of x-ray detection, we have calculated the SNR for a 1% variation in tissue attenuation for different x-ray energies (Fig. 12). The curves were generated by calculating the difference in the detected number of x-ray photons for a 1% change in attenuation at a given energy, then dividing the difference by the square root of the number of incident x-ray photons. The incident flux was adjusted to keep the dose constant at 30 mrad. The calculated values are scaled to one measurement; the number of x-ray photons/pixel under the breast and the number in the area outside of the breast, for a 6 cm breast at 30 kVp, Rh/Rh, at a 30 mrad dose. (We assume the attenuation is proportional to $(\mathrm{kVp})^{1/3}$ and the detector is equally efficient at all energies). This model is relatively crude; it does not include scatter, beam hardening, or detector noise. The model does, however, illustrate that for a given breast thickness there is an optimum x-ray energy below which the SNR falls off rapidly. The difference in the peak locations of the curves plotted in Fig. 12 shows that for a 6 cm compressed breast there is no single optimum energy for projections at both normal incidence and at 45°, and suggests that using voltages higher than those used for conventional mammography will be advantageous when the x-ray path length increases beyond ~6 cm.

Utilization of pixel binning may be a useful way to obtain

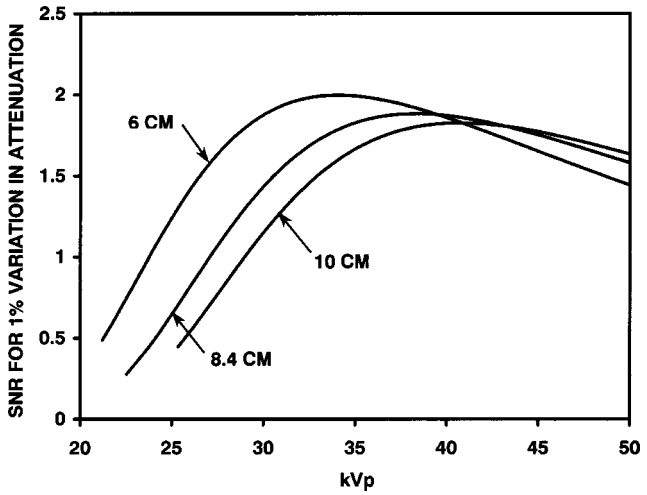

FIG. 12. Calculated signal-to-noise ratio in a 0.1 mm^2 pixel, plotted as a function of kVp, for a 1% change in attenuation for 6, 8.4, and 10 cm x-ray path lengths. The modeled flux at each energy is adjusted to keep the dose constant (30 mrad).

multiple-view volumetric data sets with reasonable dose at the expense of spatial resolution. This technique is implemented in a straightforward manner when using CCD-based detectors, for which on-board binning is easily done. Use of this approach with other detector technologies such as flat panel detectors is less clear. The inherent structure of the flat panel allows rows to be binned (by switching on multiple TFT rows simultaneously), but columns cannot be binned directly. However, because we are most interested in binning in only the *Z* dimension, this in itself is not a serious limitation. Because the dark noise is significantly less than the read noise in this detector for integration times of ~0.1 s, pixel binning would result in reduced noise.

Image reconstruction routines must be relatively rapid if these methods are to be used routinely. The ML-EM reconstruction calculations for the images in Fig. 10 (2000 $\times$1000$\times$50 pixels, 8 iterations) required ~2 h of computer time on a Pentium 900 MHz single-processor PC with 2 Gbytes of memory. We did not attempt to minimize the time. Algorithms more appropriate for clinical use would take advantage of a computer cluster with multiple, faster CPUs, precompute transformation matrices, and use faster-converging techniques like Iterative Coordinate Descent.[34–37] These modifications should reduce computation time by a factor of ~100, allowing the reconstruction to be calculated in minutes rather than hours.

The 3D reconstruction methods we have presented may make the radiologist's detection and diagnosis of breast cancer more accurate than would be possible with standard two-view projection mammography. Because the challenge of detecting cancer is greater for women and who have dense breast tissue, the method could be of particular benefit to younger women. In addition, the presentation of data in tissue layers should simplify the tasks of feature recognition and classification in computer aided diagnosis, because artifactual density arising from the superposition of overlapping

independent features in conventional mammography will be reduced in the 3D reconstruction.

ACKNOWLEDGMENTS

This work was funded by the National Institutes of Health, National Cancer Institute, Grant Nos. CA66232 and CA69452, by U.S. Army Grant Nos. DAMD 17-98-8329 and DAMD 97-1-7144.

[a]Author to whom all correspondence should be addressed: electronic mail: phillips@brandeis.edu

[1] R. A. Crowther, D. J. DeRosier, and A. Klug, ''The reconstruction of a three-dimensional structure from projections and its application to electron microscopy,'' Proc. R. Soc. London, Ser. A **317**, 319–340 (1970).

[2] T. Wu, ''Three dimensional mammography reconstruction using low dose projection images,'' Ph.D. thesis, Brandeis University, 2002.

[3] A. D. Maidment, E. F. Conant, S. A. Feig, C. W. Piccoli, and M. Albert, ''3-dimensional analysis of breast calcifications,'' in *Digital Mammography '96*, edited by K. Doi, M. L. Geiger, R. M. Nishikawa, and R. A. Schmidt (Elsevier Science, Amsterdam, 1996), pp. 245–250.

[4] L. T. Niklason, B. T. Christian, L. E. Niklason, D. B. Kopans, D. E. Castleberry, B. H. Opsahl-Ong, C. E. Landberg, P. J. Slanetz, A. A. Giardino, R. M. Moore, D. Albagi, M. C. DeJule, P. A. Fitzgerald, D. F. Fobare, B. W. Giambattista, R. F. Kwasnick, J. Liu, S. J. Lubowski, G. E. Possin, J. F. Richotte, C.-Y. Wei, and R. F. Wirth, ''Digital tomosynthesis in breast imaging,'' Radiology **205**, 399–406 (1997).

[5] S. Suryanarnyannan, A. Karellas, S. Vedantham, S. J. Glick, C. J. Orsi, and R. L. Weber, ''Comparison of contrast-detail characteristics of tomosynthetic reconstruction techniques for digital mammography,'' Radiology **213**, 368–369 (1999).

[6] A. Kak and M. Slaney, *Principles of Computerized Tomographic Imaging* (IEEE, New York, 1988).

[7] B. S. Schaller, T. Flohr, K. Klingenbeck, J. Krause, T. Fuchs, and W. A. Kalender, ''Spiral interpolation algorithm for multi-slice spiral CT. I. Theory,'' IEEE Trans. Med. Imaging **19**, 822–834 (2000).

[8] D. Hui Hu, ''Multi-slice helical CT: Scan and reconstruction,'' Med. Phys. **26**, 5–18 (1999).

[9] R. M. Nishikawa and M. J. Yaffe, ''Signal-to-noise properties of mammographic film-screen systems,'' Med. Phys. **12**, 32–39 (1985).

[10] M. B. Williams, P. Simoni, L. Smilowitz, M. Stanton, and W. Phillips, ''Analysis of the detective quantum efficiency of a developmental detector for digital mammography,'' Med. Phys. **26**, 2273–2285 (1999).

[11] K. Lange and R. Carson, ''EM reconstruction algorithms for emission and transmission tomography,'' J. Comput. Assist. Tomogr. **8**, 306–316 (1984).

[12] H. M. Hudson and R. S. Larkin, ''Accelerated image reconstruction using ordered subsets of projection data,'' IEEE Trans. Med. Imaging **13**, 601–609 (1994).

[13] K. Lange and J. Fessler, ''Globally convergent algorithms for maximum a posteriori transmission tomography,'' IEEE Trans. Med. Imaging **4**, 1430–1438 (1995).

[14] H. Guan and R. Gordon, ''Computed tomography using algebraic reconstruction techniques (ARTs) with different projection access schemes: A comparison study under practical situations,'' Phys. Med. Biol. **41**, 1727–1743 (1996).

[15] J. Skilling and R. K. Bryan, ''Maximum entropy image reconstruction: general algorithm,'' Mon. Not. R. Astron. Soc. **211**, 111–124 (1984).

[16] T. Herbert and R. Leahy, ''A generalized EM algorithm for 3D Bayesian reconstruction from Poisson data using Gibbs priors,'' IEEE Trans. Med. Imaging **8**, 194–202 (1989).

[17] R. L. White, ''Image restoration using the damped Richardson–Lucy method,'' in *The Restoration of HST Images and Spectra III, Proceedings of the Space Telescope Science Institute*, Baltimore MD, 18–19 November, 1993, edited by R. J. Hanisch and R. L. White (Space Telescope Science Institute, Bethesda, MD, 1993), pp. 58–63.

[18] J. Frank, *Electron Tomography: Three Dimensional Imaging with the Transmission Electron Microscope* (Plenum, New York, 1992).

[19] E. U. Mumcuoglu, R. M. Leahy, Z. Zhou, and S. R. Cherry, ''A phantom study of the quantitative behavior of Bayesian PET reconstruction methods,'' IEEE Nucl. Sci. Symp. Med. Imaging Conf. **3**, 1703–1707 (1995).

[20] P. A. Jansson, ''Modern constrained nonlinear methods,'' in *Deconvolution of Images and Spectra*, edited by P. A. Jansson (Academic, New York, 1997), pp. 107–181.

[21] C. Kamphuis and F. Beekman, ''Accelerated iterative transmission CT reconstruction using ordered subsets convex algorithm,'' IEEE Trans. Med. Imaging **7**, 1101–1105 (1998).

[22] W. Phillips, M. Stanton, D. O'Mara, Y. Li, I. Naday, and E. Westbrook, ''CCD-based detector for crystallographic applications using laboratory x-ray sources,'' Proc. SPIE **2009**, 133–138 (1993).

[23] S. Vedantham, A. Karellas, S. Suryanarayanan, D. Albagli, S. Han, E. J. Tkaczyk, C. E. Landberg, B. Opsahl-Ong, P. R. Granfors, I. Levis, C. J. D'Orsi, and R. E. Hendrick, ''Full breast digital mammography with an amorphous silicon-based flat panel detector: Physical characteristics of a clinical prototype,'' Med. Phys. **27**, 558–567 (2000).

[24] M. G. Bulmer, *Principles of Statistics* (Dover, New York, 1967), pp. 102–103.

[25] A. Papoulis, *Probability, Random Variables and Stochastic Processes*, 3rd ed. (McGraw–Hill, New York, 1991).

[26] G. H. Golub and C. F. Van Loan, *Matrix Computation* (John Hopkins University Press, Baltimore, 1989).

[27] A. P. Dempster, N. M. Laird, and D. B. Rubin, ''Maximum likelihood from incomplete data via the EM algorithm,'' J. R. Stat. Soc. Ser. B. Methodol. **39**, 1–3 (1977).

[28] L. Shepp and Y. Vardi, ''Maximum likelihood reconstruction for emission tomography,'' IEEE Trans. Med. Imaging **MI-1**, 113–122 (1982).

[29] D. Yu and J. Fessler, ''Edge-preserving tomographic reconstruction with nonlocal regularization,'' IEEE Trans. Med. Imaging **21**, 159–173 (2002).

[30] J. A. Delaney and Y. Bresler, ''Globally convergent edge-preserving regularized reconstruction: An application to limited-angle tomography,'' IEEE Trans. Image Process. **7**, 204–221 (1998).

[31] G. L. Zeng, C. Bai, and G. T. Gullberg, ''A projector/backprojector with slice-to-slice blurring for efficient three-dimensional scatter modeling,'' IEEE Trans. Med. Imaging **18**, 722–732 (1999).

[32] M. Endo, T. Tsunoo, and N. Nakamori, ''Effect of scatter radiation on image noise in cone-beam CT,'' Proc. SPIE **3977**, 514–521 (2000).

[33] J. H. Siewerdsen and D. A. Jaffray, ''Optimization of x-ray imaging geometry (with specific application to flat-panel cone-beam computed tomography,'' Med. Phys. **27**, 1903–1914 (2000).

[34] J. A. Fessler, ''Statistical reconstruction methods for transmission tomography,'' in *Handbook of Medical Imaging*, edited by M. Sonka and L. M. Fitzpatrick (SPIE, Bellingham, WA, 2000), Vol. 2, pp. 1–70.

[35] K. D. Sauer, S. Borman, and C. A. Bouman, ''Parallel computation of sequential pixel updates in statistical tomographic reconstruction,'' IEEE Int. Conference Image Processing **2**, 93–96 (1995).

[36] E. C. Frey, Z-W. Ju, and B. M. W. Tsui, ''An investigation of two approximation methods for improving the speed of 3D iterative reconstruction-based scatter compensation,'' in *Three-dimensional Image Reconstruction in Radiation and Nuclear Medicine*, edited by A. Grangeat and J. L. Amans (Kluwer Academic, Amsterdam, 1996), pp. 177–193.

[37] J. A. Fessler, E. P. Ficaro, N. H. Clinthorne, and K. Lange, ''Grouped-coordinate ascent algorithms for penalized-likelyhood transmission image reconstruction,'' IEEE Trans. Med. Imaging **16**, 166–175 (1997).